Proceedings of the 5th International Conference on Nonlinear Dynamics
ND-KhPI2016
September 27-30, 2016, Kharkov, Ukraine

Improvement of Piezoelectric Energy Harvester Efficiency Through Optimal Patch Configuration

Julian S. Gosliga[1*], Olga A. Ganilova[1]

Abstract
The aim of this paper is to explore how to improve the efficiency of a vibrating hybrid energy harvester through changing the patch configuration. The results of this work identify the patch configuration that maximises output while using the same amount of piezoelectric material. Using 6 patches was found to be the most efficient when looking at the energy output from a single cycle. Stress distributions generated using ANSYS show that this was because the patches were all located in areas of high stress. The 2 patch configuration resulted in the highest energy conversion at low frequencies (peak loss factor <50Hz) while the performance of the 6 patch configuration was characterised by high energy conversion over a wider range of frequencies.

Keywords
Energy harvesting, hybrid, piezoelectric, shape-memory, patch optimisation

[1] Department of Mechanical Engineering, University of Sheffield, Mappin Street, Sheffield, S13JD, *UK*
*** Corresponding author:** jsgsoliga1@sheffield.ac.uk

Introduction

Advances in the fields of low power electronics and energy harvesting have made it possible to create self-powered sensors that are only a few millimetres in scale [1]. These self-powered sensors can be used for condition-monitoring in remote or inaccessible locations. These devices could be used in medical implants in order to power pacemakers [2]; or sensors which could monitor for early warning signs of disease.

These self-powered devices harvest energy from their environment instead of using batteries. Energy harvesters for powering medical implants have to be small so they are not invasive, hence it is obvious that materials with high work densities are needed, such as piezoelectric materials [3] or shape memory alloys (SMA). Increasing the efficiency allows the harvester to be made smaller, while still achieving the same output. Most often, piezoelectric materials are used to convert mechanical energy into electrical energy through the direct piezoelectric effect (DPE) [4]. Unlike thermoelectric generators, which require large fixed temperature gradients, piezoelectric materials can convert fluctuating temperature into electrical energy via the pyroelectric effect [5]. Piezoelectric materials are also used to control vibrations [6] by converting mechanical energy into electrical energy via the DPE and then dissipating this energy through a resistor or inductor. In this paper the patches are assumed to made of the piezoelectric ceramic lead zirconate titanate (PZT).

Thermal energy can be converted into mechanical energy the shape memory effect (SME). The SME has not been widely explored for energy harvesting as it does not directly convert thermal energy into electrical energy. The mechanical energy is typically used to control vibration or modify the shape and mechanical properties of a structure [7,8]. The SME is generally activated using an external power source, instead of using energy from the environment.

An energy harvester which uses a hybridisation of the DPE, SME and pyroelectric effects could achieve a greater energy output than either a thermoelectric or pyroelectric generator of comparable size [9]. Such a device would primarily rely on temperature fluctuations found in the body, as opposed to large fixed temperature gradients. Additionally, the reliance on the frequency of the

temperature fluctuations could be reduced by using the SME to increase the energy output per cycle [10]. There have been others attempts to combine SMA and piezoelectric for various applications, both experimentally and theoretically [11–13]. However, there has been little attempt to systematically optimise these devices to improve size and energy output for powering a medical implant

The aim of this work is to study how the number of PZT patches in a hybrid energy harvesting device (HEHD) affects the performance of the device by using static and dynamic finite element (FE) models using the commercial software package, ANSYS. The device under consideration consists of both an SMA and piezoelectric element, though this paper focuses on the piezoelectric harvester. The stress distribution and energy output over a single cycle for the various patch configurations was examined and compared. The dynamic behaviour of the PZT patches was simulated using a shunted piezoelectric damping model as described in [6]. This was then used to study the effect of patch number on the dynamic performance of the energy harvester. The amplitude frequency response functions (FRF) for the various patch configurations were compared to find trends.

1. Development of the finite element model

The HEHD under consideration is based on the design developed and described in detail in [14]. The harvester uses a contracting SMA actuator to deform a piezoelectric element (similar to that shown in Figure 1) as the device heats up, with the elastic energy stored in the piezoelectric element providing the restoring force.

The dimensions for the FE model are given in Table 1. In this composite, the PZT is included in the two outermost plies and arranged in rectangles. The number of patches is varied, thus changing the patch configuration and energy output of the device. Figure 1 shows the schematic for a piezoelectric element containing 4 patches. For the 2 patch and 6 patch configurations (models) the dimension c was 0.09m and 0.03m respectively, with equal spacing between the patches and edge of the piezoelectric element. The size of the patches in each model was chosen so that the volume fraction of PZT relative to the CFRP host material was kept the same.

1.1. Energy output

The total stresses across all of the elements in each patch was taken and then divided by the amount of elements to give an average stress value for each patch. To calculate the total energy, the average stress in both the x and y directions were calculated from the FE model and used along with Equation (1). This expression was altered depending on the number of patches and their poling direction.

$$U = 4\sum_{m=1}^{2}\left[\frac{1}{2}\int_{v_1}\left(d_{33}g_{33}\sigma_x^2 + d_{31}g_{31}\sigma_y^2\right)dv_1 + \frac{1}{2}\int_{v_2}\left(d_{33}g_{33}\sigma_y^2 + d_{31}g_{31}\sigma_x^2\right)dv_2\right] \tag{1}$$

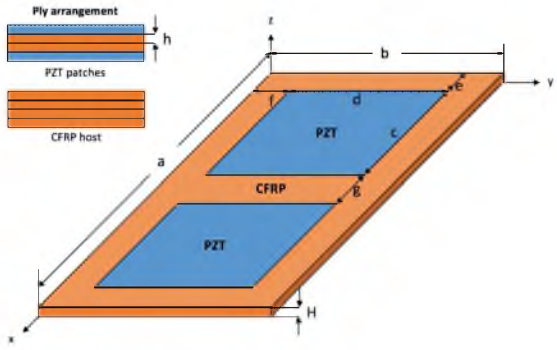

Figure 1. A schematic showing the dimensions and ply arrangement for the multilayered composite plate with embedded PZT patches

Table 1. List of dimensions for the HEHD as well as material properties for both materials

Material	Parameter	Value	Units
CFRP	Length a	0.1	m
	Width b	0.05	m
	Overall thickness H	0.0005	m
	Young's Modulus	$70.0\,10^9$	N/m^2
	Poisson's Ratio	0.10	---
	Density	1600	kg/m^3
PZT	Patch length c	0.045	m
	Patch width d	0.04	m
	Patch thickness h	0.000125	m
	Spacing e	0.0025	m
	Spacing f	0.005	m
	Separation g	0.005	m
	Short circuit stiffness	$65.5\,10^9$	N/m^2
	Open circuit stiffness	$74.0\,10^9$	N/m^2
	Poisson's Ratio	0.31	---
	Density	7800	kg/m^3
	Piezoelectric charge constant d_{31}	$-175\,10^{-12}$	C/N
	Electromechanical coupling factor k_{31}	0.34	---

1.2. Damping effect

To examine how the PZT patches would affect the damping characteristics of the harvester, the patches were considered as though there was a resistor attached, to simulate the effect of the harvesting circuitry. The energy that is dissipated across the resistor represents the energy that would be harvested from the system and can be represented by a loss factor. The stiffness of a piezoelectric material is altered depending on the charge across it, as any charge generates stress within the material. This generated stress can either assist or oppose external forces. Both the stiffness and loss factor can be shown to be complex and frequency dependant.

Due to the electromechanical coupling of the system, it is necessary to use both the mechanical and electrical impedances to give an expression for the stiffness. The subscripts *i* and *j* denote the generated electric field (*z*-axis) and uniaxial loading direction (*x*-axis) respectively. As shown in [6], the non-dimensional $\bar{Z}_{jj}^{ME}(s)$ mechanical impedance for the shunted piezoelectric can be expressed in the Laplace domain,

$$\bar{Z}_{jj}^{ME}(s) = (1 - k_{ij}^2)/\left[1 - k_{ij}^2 \bar{Z}_i^{EL}(s)\right] \tag{2}$$

where k_{ij} is the coupling factor of the piezoelectric material, given in Table 1 and $\bar{Z}_i^{EL}$ is the non-dimensional electrical impedance and is given by

$$\bar{Z}_i^{EL}(s) = R_i C_{pi}^T s/\left(R_i C_{pi}^T s + 1\right) \tag{3}$$

where R_i is the resistance of the system (an arbitrary value of 100kΩ was used). The capacitance of the piezoelectric patch at constant stress C_{pi}^T can be determined from the area of the patch A_i, the dielectric constant at constant stress ε_i^T, and thickness of the patch L_i:

$$C_{pi}^T = A_i \varepsilon_i^T / L_i \tag{4}$$

Equation (3) can be substituted into Eq. (2) to give the following expression for the non-dimensional mechanical impedance of a resistive shunted piezoelectric

$$\bar{Z}_{jj}^{RES}(\omega) = 1 - k_{ij}^2/\left(1 + \mathrm{i}\rho_i\right) \tag{5}$$

where ρ_i is the non-dimensional frequency, defined by

$$\rho_i = R_i C_{pi}^S \omega = \omega/\omega_d \tag{6}$$

where ω is the input frequency, ω_d is the damped natural frequency and C_{pi}^S is the capacitance of the PZT patch at constant strain, which is given by

$$C_{pi}^S = C_{pi}^T\left[1 - k_{ij}^2\right] \tag{7}$$

Since the mechanical impedance is primarily a stiffness, the impedance can be represented as a complex modulus [6],

$$\bar{Z}_{jj}^{ME}(s) = \bar{E}_{jj}(\omega)\left[1 + \mathrm{i}\eta_{jj}(\omega)\right] \tag{8}$$

where $\bar{E}$ is the ratio of shunted stiffness to open circuit stiffness and η is the material loss factor.

$$\eta(\omega) = \frac{\mathrm{Im}\{\bar{Z}^{ME}(s)\}}{\mathrm{Re}\{\bar{Z}^{ME}(s)\}} \qquad \bar{E} = \mathrm{Re}\left\{\bar{Z}^{ME}(s)\right\} \tag{9a,b}$$

Comparing Eq (6) and Eq (2), and applying Eqs (9a,b), it is possible to obtain the following frequency dependent expressions,

$$\eta_{jj}^{RES}(\omega) = \rho_i k_{ij}^2/\left\{\left(1 - k_{ij}^2\right) + \rho_i^2\right\} \qquad \bar{E}_{jj}^{RES}(\omega) = 1 - k_{ij}^2/\left(1 + \rho_i^2\right) \tag{10a,b}$$

The values for both the loss factor and stiffness ratio were calculated over a set frequency interval in MATLAB to create a data table. These values were then used to create a viscoelastic material model in ANSYS which allowed for variable damping and complex stiffness to be taken into account.

The equivalent damping ratio to be used for the linear damping model was calculated from the maximum loss factor using the following approximation $\eta \approx 2\zeta$ [15].

2. Results and discussion

2.1. Stress distribution

The stress distribution in the *x*-direction (or *j*th direction) for each model is presented in Fig. 2. The surfaces shown are those with the highest average stress for each respective model; this is taken as the 'top' surface.

As can be seen in Fig. 2, each model has a similar pattern with the highest stresses at the centre and edges of the harvester. The stress transitions from either tension or compression, changing sign along the length of the harvester. With 2 patches (Fig. 2a), the patches extend across almost the entire distribution. However, there is a larger area in tension (red) than in compression (blue) and so the stress does not cancel out. On the other hand, in the 4 patch model (Fig. 2b), the patches fall on the areas where the stress transitions from tension to compression and so the average stress is lower.

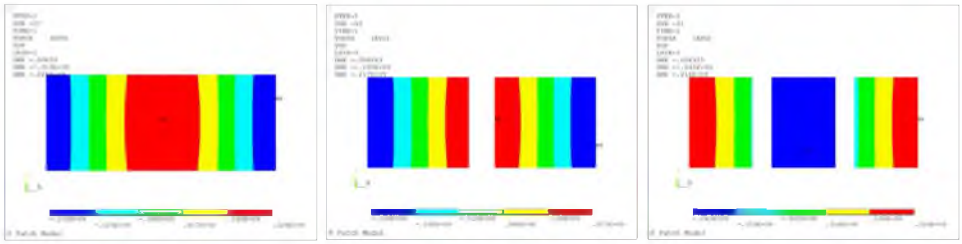

Figure 2. Stress distribution in the x-direction in the patches on the top layer for the (a) 2 patch, (b) 4 patch, (c) 6 patch models. Blue represents areas in compression and red representes areas in tension

Table 2 lists the energy output for each patch configuration model. As it can be seen the 6 patch model produced 5 times the energy of the 2 patch model, which itself produced roughly 3 times the amount of energy of the 4 patch harvester. In Table 2 the device with the highest output is the 6 patch (Fig. 2c), where the patches are located close to an area of high stress. Since the input was the same for all three devices, it can be said that the 6 patch was the most efficient.

Table 2. Energy output each of the patch configurations

Model	2 Patch	4 Patch	6 Patch
Energy output	462.11 μJ	165.45 μJ	2300 μJ

2.2. Loss factor and stiffness ratio analysis

The variation in the loss factor (Fig. 3) and stiffness ratio (Fig. 4) are both shown over the frequency range 0-300Hz.

Figure 3 shows that as the number of patches increases, the frequency at which the peak loss factor occurs increases. The peak also becomes less pronounced as the number of patches increases, with the loss factor decreasing more gradually from its peak value. By examining Eq. (10a) and Eq. (6) together it can be seen that the relationship between frequency and loss factor is affected by the capacitance, which varies with the patch dimensions. The loss factor – frequency relationship can be tuned by adjusting the resistance. Optimising this relationship is important for good efficiency, as the loss factor represents the amount of mechanical energy converted to useful electrical energy. For the same material and loading case (transverse or longitudinal), the peak loss factor is the same.

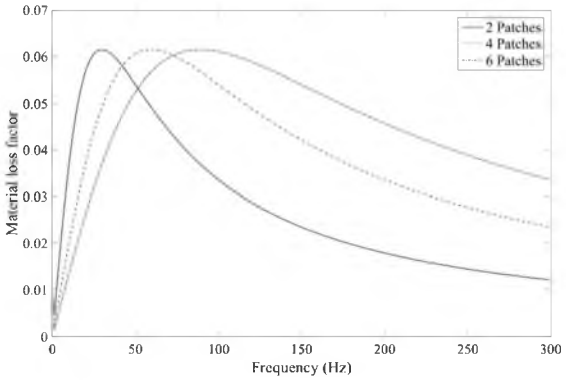

Figure 3. Variation in loss factor with respect to frequency for the 2 (solid), 4 (dash) and 6 (dash-dot) patch models calculated using Eq. 10a

Figure 4 shows the rate at which the stiffness of the PZT patches reaches the open circuit stiffness decreases as the number of patches increases. The stiffness in the shunted damping model approaches the open circuit stiffness (7.4GPa) as the frequency increases, while the other models use the lower short circuit stiffness (6.5GPa). The relationship between the stiffness and frequency is influenced by Eq. (6) and, as can be seen in Fig. 4, smaller patches result in a lower stiffness.

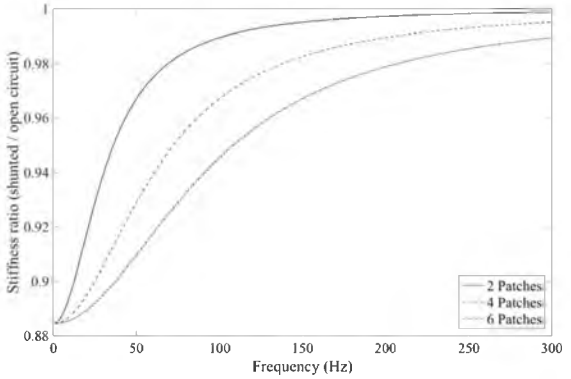

Figure 4. Variation in stiffness ratio with respect to frequency for the 2 (solid), 4 (dash) and 6 (dash-dot) patch models calculated using Eq. 10b

2.3. Damping effect analysis

Figure 5 shows a comparison of the amplitude FRFs for the case where there is no damping; the case where the damping ratio is constant chosen to be $\zeta = 0.03$ as a numerical example; and the case where the shunted damping model is used. The resonance occurs at the same frequency for both the undamped and linearly damped model, as expected the peak amplitude is reduced in the damped case. The resonance for the shunted damping model occurs at a slightly higher frequency and has a peak amplitude between that of the undamped and linearly damped model.

The variation in damping between the shunted model and linear model, means that the dynamic behaviour of the harvester is different. This can be seen in Fig. 5, where the amplitude of the harvester is higher than that of the linearly damped system, suggesting that there is less damping. The reason for this is that the damping ratio in this model was based on the maximum loss factor for the 4 patch model $\eta = 0.06$, whilst close to the resonant frequency, the loss factor for the shunted damping model is roughly 0.04. The peak amplitude in Fig. 5 for the shunted damping model is shifted to the right, one explanation for this could be that the stiffness was higher for the undamped and linearly damped models, resulting in a higher resonant frequency.

Figure 6 shows a comparison between all three of the patch configurations under consideration (HEHD with 2, 4 and 6 patches embedded), where the stiffness and loss factor values have been calculated using the shunted damping model described in Section 1.2. Based on the trends seen in Fig. 5 and Fig. 4, one could make the prediction that the 2 patch model should exhibit the highest resonant frequency followed by the 4 patch model. In this case the 6 patch would have the lowest resonant frequency. Figure 6 shows no such trend. In addition to this, the models all appear to have similar damping, despite differences in loss factor. This shows that predicting the effect that damping, stiffness and patch location has on the dynamic behaviour of the device is not straightforward. This could present difficulties when trying to tune the system, although if the effect of patch configuration could be accurately modelled, it could represent another dimension for designers to use when optimising a system.

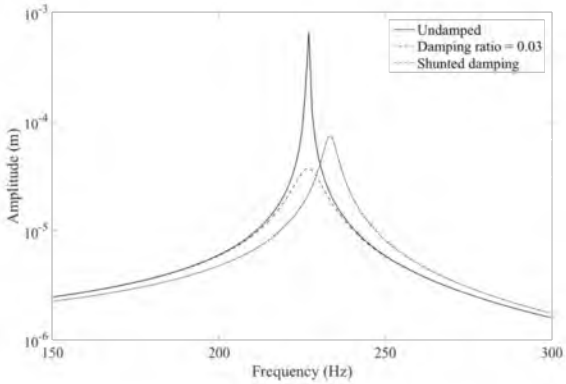

Figure 5. Amplitude FRF for no damping (solid), linear damping (dash) and shunted damping (dash-dot) for the 4 patch configuration model

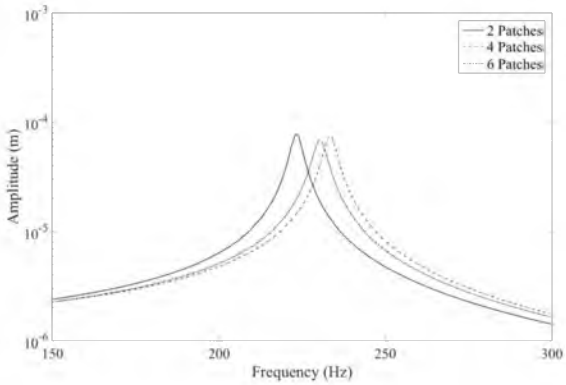

Figure 6. Amplitude FRF for the 2 (solid), 4 (dash) and 6 (dash-dot) patch models with shunted damping

Conclusions

An analysis of the static and dynamic behaviour for different patch configurations using the HEHD model discussed in [14] has been performed. The best energy output for the device relies on ensuring the patches are close to stress concentrations found in the harvester, as this results in higher average stresses across the patches. The 6 patch design was the most efficient in the static case due to the fact that patches were all located in the areas where the stress was high. The least effective configurations had patches located in areas where the sign of the stress changed from tension to compression, which meant lower average stresses.

The loss factor represents the amount of mechanical energy which is converted and then dissipated in the device in the form of electrical energy. A higher loss factor means a greater amount of the mechanical energy is being converted. Therefore, to achieve optimal output for the device, tuning has to be applied to match the frequency where the peak loss factor occurs with the driving frequency. Different patch configurations have differently shaped loss factor curves, making each one more effective for specific application. For example, the 6 patch model, appears to give a wider peak, and so would be useful for broadband energy harvesting. Patch configuration represents another dimension to consider when designing a device, although the dynamic effects are difficult to predict due to non-linear frequency dependant behaviour.

References

[1] He, C., Kiziroglou, M.E., Yates, D.C., Yeatman, E.M. A MEMS self-powered sensor and RF transmission platform for WSN nodes. *IEEE Sensors Journal*, 2011; 11(12):3437-3445.

[2] Dagdeviren, C., Yang, B.D., Su, Y., et al. Conformal piezoelectric energy harvesting and storage from motions of the heart, lung, and diaphragm. *Proceedings of the National Academy of Sciences of the United States of America*, 2014; 111(5):1927-1932.

[3] Roundy, S., Wright, P.K., Rabaey, J. *A study of low level vibrations as a power source for wireless sensor nodes.* Computer Communications, 2003; 26(11):1131-1144.

[4] Sodano, H.A. Generation and Storage of Electricity from Power Harvesting Devices. *Journal of Intelligent Material Systems and Structures*, 2005; 16(1):67-75.

[5] Cuadras, A., Gasulla, M., Ferrari, V. Thermal energy harvesting through pyroelectricity. Sensors and Actuators, A: Physical, 2010; 158(1):132-139.

[6] Hagood, N.W., von Flotow, A. Damping of structural vibrations with piezoelectric materials and passive electrical networks. Lopez-Higuera JM, Jones JDC, Lopez-Amo M, Santos JL, eds. *Journal of Sound and Vibration*, 1991; 146(2):243-268.

[7] Zak, A.J., Cartmell, M.P. Control of vibrations by SMA components. *2nd International Conference on Advanced Engineering Design*, 2001.

[8] Zak, A.J., Cartmell, M.P., Ostachowicz, W. Dynamics of Multilayered Composite Plates With Shape Memory Alloy Wires. *Journal of Applied Mechanics*, 2003; 70(3):313.

[9] Paradiso, J.A., Starner, T. Energy scavenging for mobile and wireless electronics. *IEEE Pervasive Computing*, 2005; 4(1):18-27.

[10] Gusarov, B., Gimeno, L., Gusarova, E., Viala, B., Boisseau, S., Cugat, O. Flexible composite thermal energy harvester using piezoelctric PVDF polymer and shape memory alloy. *IEEE Solid-State Sensors, Actuators and Microsystems (TRANSDUCERS)*, 2015:722-725.

[11] Namli, O.C., Taya, M. Design of Piezo-SMA Composite for Thermal Energy Harvester Under Fluctuating Temperature. *Journal of Applied Mechanics*, 2011; 78(3):031001.

[12] Avirovik, D., Kumar, A., Bodnar, R.J., Priya, S. Remote light energy harvesting and actuation using shape memory alloy—piezoelectric hybrid transducer. *Smart Materials and Structures*, 2013; 22(5):052001.

[13] Reddy, A.R., Umapathy, M., Ezhilarasi, D., Uma, G. Piezoelectric Energy Harvester With Shape Memory Alloy Actuator Using Solar Energy. 2015; 6(4):1409-1415.

[14] Gosliga, J.S., Ganilova, O.A. Energy Harvesting based on the Hybridisation of two Smart Materials. In: *EACS 2016 – 6th European Conference on Structural Control. Sheffield, UK*; 2016.

[15] Graesser, E.J., Wong, C.R. Relationship of traditional damping measures for materials with high damping capacity: A review. In: *Symposium on M3D: Mechanics and Mechanisms of Material Damping.* ; 1992:316-343.